THE JOURNAL OF PHYSICAL CHEMISTRY C
A JOURNAL OF THE AMERICAN CHEMICAL SOCIETY

pubs.acs.org/JPCC
Article

Hydrostatic Pressure-Driven Band Gap Tuning and Self-Trapped Exciton Formation in $(4FPEA)_2SnBr_4$ Halide Perovskite

Rafał Bartoszewicz,* Jakub Ziembicki, Ewelina Zdanowicz, Artur P. Herman, Jarosław Serafińczuk, Jesús Sánchez-Diaz, Samrat Das Adhikari, Iván Mora-Seró, and Robert Kudrawiec

Cite This: https://doi.org/10.1021/acs.jpcc.6c02337

Read Online

ACCESS | Metrics & More | Article Recommendations | Supporting Information

ABSTRACT: Two-dimensional tin-halide perovskites provide a highly tunable platform for exciton−phonon coupling and local lattice distortions, enabled by their intrinsically soft lattice. We report a combined temperature- and pressure-dependent photoluminescence study of the layered perovskite $(4FPEA)_2SnBr_4$. At room temperature, its optical response is dominated by near-band-edge (NBE) excitons, which red-shift linearly under hydrostatic pressure up to ∼3 GPa, indicating a rigid band-edge behavior without phase transitions. Cooling reveals a broad, strong Stokes-shifted self-trapped exciton (STE) emission, evidencing a crossover from delocalized to self-localized excitonic states. Strikingly, while NBE emission red-shifts under pressure, STE emission exhibits an anomalous blue shift, reflecting pressure-induced modification of the exciton−phonon energy landscape. In contrast, the iodide analogue $(4FPEA)_2SnI_4$ shows no STE emission under identical conditions, highlighting the critical role of lattice rigidity and dielectric screening in stabilizing self-trapped excitons.

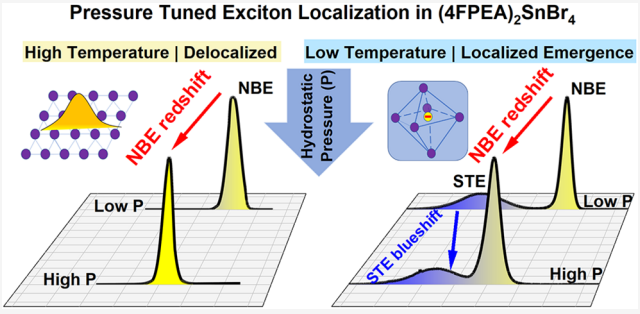

INTRODUCTION

Tin-based halide perovskites have emerged as promising lead-free optoelectronic materials, offering reduced toxicity with strong light−matter interactions and long carrier lifetimes.[1−6] Among them, two-dimensional (2D) Sn-based halide perovskites exhibit pronounced quantum confinement and enhanced excitonic localization,[7−9] making them attractive platforms for studying exciton−phonon coupling phenomena.[10−13] In these materials, the interplay between the electronic structure and lattice dynamics governs key processes such as exciton self-trapping, radiative recombination, and carrier−phonon interactions.[14−16]

In particular, the coexistence and competition between free excitons and self-trapped excitons (STEs) have attracted growing attention,[9,17] as STE formation is often associated with large Stokes shifts (200−500 meV), broadband emission (100−300 meV), and enhanced exciton−phonon coupling,[18,19] properties that are both technologically appealing and scientifically challenging to control. Here, STEs are interpreted as small polarons, excitons that become tightly localized through strong short-range electron−phonon coupling and consequent local lattice distortion, in contrast to more delocalized large polarons associated with the free excitonic state.[19,20] In principle, STEs can be further categorized into those that arise intrinsically from the host lattice and those that are bound to defects or lattice imperfections. In high-quality samples where defect densities are minimal, defect-bound STE signatures are often not resolvable, leaving primarily an intrinsic small polaron STE behavior in the optical response.

Exciton self-trapping in halide perovskites is generally attributed to strong coupling between electronic excitations and local lattice distortions.[18] While STE emission has been widely reported in low-dimensional and all-inorganic halide perovskites, its emergence is highly sensitive to lattice rigidity, dielectric screening, chemical composition, and temperature.[19] Despite extensive experimental and theoretical efforts, a unified understanding of how external perturbations modulate the balance between delocalized and localized excitonic states remains incomplete.[21,22] Hydrostatic pressure provides a powerful, continuous, and reversible means of tuning interatomic distances, orbital overlap, and phonon spectra without introducing chemical disorder.[23] Yet, pressure-dependent behavior of excitons in layered tin-based halide perovskites remains comparatively unexplored.

Notably, Sn-based halide perovskites demonstrate remarkable resilience to external stimuli such as hydrostatic pressure

Received: April 12, 2026
Revised: July 8, 2026
Accepted: July 14, 2026

and temperature.[24,25] These stimuli can significantly modulate crystallographic and electronic structures, leading to band gap renormalization, photoluminescence (PL) enhancement, defect-assisted recombination, or even amorphization.[23] In many cases, compression activates new emissive channels or enhances STE formation,[22,26−28] often accompanied by structural instabilities. However, such responses are highly material specific and dependent sensitively on halide chemistry, lattice stiffness, and intrinsic structural softness. Understanding the behavior of these materials under extreme perturbations is therefore important for the development of next-generation perovskite-based devices,[29,30] including stimuli-responsive optoelectronic, temperature sensing, mechanical stress detection, and flexible electronics.[31−33]

4-Fluorophenethylammonium tin bromide ($(4FPEA)_2SnBr_4$) is a recently developed 2D Sn-based halide perovskite.[34] While its structure allows for straightforward optoelectronic characterization, its fundamental optical properties have not yet been reported. In comparison, the closely related $(PEA)_2SnBr_4$ exhibits a direct band gap of ∼2.7 eV and photoluminescence around ∼2.64 eV,[35] suggesting that similar optical behavior may be anticipated in the 4F-substituted derivative. Studies on layered Sn halide perovskites further indicate that both the halide composition and the organic spacer modulate the band gap and emission characteristics.[36] Despite this, the excitonic response of $(4FPEA)_2SnBr_4$ under external perturbations remains largely unexplored.

In this Article, we present a comprehensive investigation of the excitonic response of $(4FPEA)_2SnBr_4$ under combined control of temperature and hydrostatic pressure. By tracking its PL spectra from room temperature down to cryogenic temperatures and pressures up to ∼3 GPa, we uncover a strikingly rigid high-temperature excitonic response, characterized by a single near-band-edge (NBE) emission. Here, the high-energy emission close to the optical band edge is referred to as NBE excitonic emission and is commonly attributed to free exciton recombination. This emission red-shifts linearly with pressure without any anomalous spectral broadening, intensity enhancement, or evidence of phase transitions what is in line with behavior reported for other perovskites. In contrast, at low temperatures, a broad STE emission emerges exclusively in the bromide compound, exhibiting an anomalous blue shift under compression. Direct comparison with iodide analogues shows that STE emission is entirely suppressed in softer, more strongly screened lattices.

METHODS

Materials

Acetic acid (AcOH, 99−100%), hydrobromic acid (HBr; 48 wt % in H_2O), hydroiodic acid (HI; 57 wt % in H_2O, distilled, stabilized, 99.95%), and hypophosphorous acid (H_3PO_2; 50 wt % in H_2O) were purchased from Sigma-Aldrich. Tin(II) oxide (SnO; 99%) was purchased from Alfa Aesar. 4-Fluorophenethylamine (4FPEA; 98%) was purchased from TCI. All materials were used as received with no further purifications.

Synthesis of $(4FPEA)_2SnBr_4$ Microcrystal Powder

Synthesis of $(4FPEA)_2SnBr_4$ was carried out following the literature report.[34] A mixture consisting of 3 mL of acetic acid and 0.3 mL of hydrobromic acid (HBr) was combined in a three-necked flask under an inert nitrogen (N_2) atmosphere. The mixture was stirred at room temperature for 30 min. Next, 134 mg of tin(II) oxide (SnO) was introduced into the flask, and the temperature was gradually increased to 100 °C. The solution was stirred for an additional 30 min until it developed a white color. Subsequently, 0.26 mL of 4-fluorophenylethylamine (4FPEA) was added, and the reaction temperature was further raised to 135 °C. The mixture was maintained under these conditions for 15 min. Upon completion of the reaction, the solution was rapidly cooled using an ice bath for approximately 2 min; in this step, the microcrystalline products were formed, having a green-yellow appearance. The resulting product was collected via vacuum suction filtration. To eliminate any excess bromide, the collected powder was washed three times with hexane, followed by additional vacuum suction filtration. Finally, the purified product was dried.

Synthesis of $(4FPEA)_2SnI_4$ Microcrystal Powder

Synthesis of $(4FPEA)_2SnI_4$ was carried out following the same procedure as $(4FPEA)_2SnI_4$. A mixture consisting of 3 mL of acetic acid, 0.2 mL of hydroiodic acid (HI), and 0.05 mL of H_3PO_2 was combined in a three-necked flask under an inert N_2 atmosphere. The mixture was stirred at room temperature for 30 min, during which a transition from a faint red to a colorless appearance indicated the stabilization of HI in the presence of H_3PO_2. Next, 134 mg of SnO was introduced into the flask, and the temperature was gradually increased to 100 °C. The solution was stirred for an additional 30 min until it developed an orange color. Subsequently, 0.26 mL of 4FPEA was added, and the reaction temperature was further raised to 135 °C. The mixture was maintained under these conditions for 15 min. Upon completion of the reaction, the solution was rapidly cooled using an ice bath for approximately 2 min. The resulting product was collected via vacuum suction filtration. To eliminate any excess iodine, the collected powder was washed three times with hexane, followed by additional vacuum suction filtration. Finally, the purified product was dried.

X-ray Diffraction (XRD) Measurement

XRD pattern of the microcrystals was measured using an X-ray diffractometer (D8 Advance, Bruker-AXS) (Cu Kα, wavelength λ = 1.5406 Å) with a Bragg angle range of 4−70° and step size of 0.05°.

In high-pressure measurements, $(4FPEA)_2SnBr_4$ was measured using a Malvern Panalytical Empyrean 3 X-ray diffractometer. An Ag X-ray tube with a $\lambda_{K\alpha I}$ wavelength of 0.559421 Å was used. The primary beam optics consisted of a 135 mm monocapillary with a diameter of 0.3 mm, while a 1Der detector was used in the diffracted beam path. The measurements were performed using an Almax mechanical diamond anvil cell, allowing pressures of up to 15 GPa to be reached.

Temperature- and Pressure-Dependent PL

PL measurements were performed in the Diacell design DAC by Almax easyLab. DAC used in this work is made of beryllium copper (BeCu) alloy, which allows us to perform measurements at cryogenic temperature (here 40 K). A diamond with 650 μm culet size was used. The pressurizing mechanism in the DAC was driven using a gas membrane. The pressure in DAC was controlled by the amount of helium injected into the gas membrane. On top of the bottom diamond culet, a gasket was placed. It is a thin sheet (ca. 50 μm thickness) of Inconel material with a central hole of about 1/3 culet size, where the sample, ruby sphere, and silicon oil were placed. Gaskets were prepared by pressing diamonds into a thin sheet, followed by

https://doi.org/10.1021/acs.jpcc.6c02337
J. Phys. Chem. C XXXX, XXX, XXX−XXX

creating a central hole using mechanical drilling. Daphne 7575 was used as the pressure-transmitting medium, which solidifies at about 5.4 GPa at room temperature. The whole setup was cooled down in a cryostat with a closed-loop liquid helium system. For PL experiments, a 405 nm continuous-wave (CW) (with a power of 100 μW) laser was used to excite the studied material. Emitted light was dispersed through a 0.5 m Andor monochromator with a 150 l/mm diffraction grating blazed at 500 nm. The signal was recorded by a Si charge-coupled device (CCD) camera cooled to 70 °C by a Peltier module. The luminescence of the ruby R1 line at 1.78 eV (at room temperature) was excited by the 532 nm CW laser, dispersed on the 600 l/mm diffraction grating blazed at 500 nm, and detected by a CCD camera. To determine the pressure value inside DAC, we detect the pressure-induced red shift of the ruby sphere R1 line with calibration taken from Shen.[37] The temperature shift correction of the R1 ruby line was taken from Datchi.[38]

Pressure-Dependent Transmission

The optical microscope NADE NMM-800TRF and Mitutoyo M PLAN APO NIR 50×/0.42 f = 200 lens were used to properly focus on the sample placed inside the DAC chamber. For transmission measurements, a halogen lamp (with a voltage of 24 V and power of 100 W) was used as a light source. Transmitted light was recorded by a StellarNet Blue-Wave UVIS 200 spectrometer with a 600 l/mm grating and a 200 nm slit with a resolution of 1.0. A Delta Optical DLT-CAM PRO 3 MP USB 3.0 camera allowed us to investigate the color change of the perovskite. To excite the R1 luminescence of the ruby, a 532 nm CW laser was used (emission power of 100 mW). In this case, an AVANTES ULS4096CL-RS-EVO with a DCL-UV/vis-200 600 l/mm diffraction grating blazed at 300 nm was used as a detector. To determine the pressure value inside DAC, we detect the pressure-induced red shift of the ruby sphere R1 line with calibration taken from Shen.[37]

Theoretical Calculations

Density functional theory (DFT) calculations were performed using the VASP package with standard Perdew, Burke, and Ernzerhof (PBE) projector-augmented wave (PAW) data sets.[39−42] Geometry optimizations were first carried out over a pressure range of 0−3 GPa using the r^{2}SCAN + rVV10 functional.[43] The optimized geometries were then used for band gap and band structure calculations. In this second step, the same functional was employed with two additional modifications. First, a uniform scissor shift of 1.1 eV was applied to the band gaps at all pressures to match the values obtained from the PBE0 functional, thereby correcting the band gap underestimation inherent to meta-generalized gradient approximation (GGA) functionals. Second, spin−orbit coupling was included, as it is known to have a significant impact on the band structure of this class of materials. All calculations used identical computational parameters: an energy cutoff of 500 eV, a Γ-centered 3 × 6 × 6 k-point mesh, a self-consistent field (SCF) energy convergence criterion of 10^{-5} eV, and a force convergence criterion of 10^{-2} eV/Å for geometry optimization. For the PBE0 calculations, k-point mesh down-sampling was applied using the VASP flag NKRED = 3.

RESULTS AND DISCUSSION

The synthesis of $(4FPEA)_2SnBr_4$ microcrystals was performed using the developed methodology elsewhere,[34] as detailed in the Methods section. To prove the formation and explore the crystallographic features of the resulting microcrystals, we performed X-ray diffraction (XRD) to identify the crystal phases obtained. Figure S1 in the Supporting Information (SI) shows the XRD pattern of the $(4FPEA)_2SnBr_4$ microcrystals, exhibiting high crystallinity and uniformity, and repetitive XRD peaks with intervals of ∼5.4°, which corresponds to the interlayer distance of the inorganic layers.

High-pressure XRD measurements were performed over a 2Θ range of 3−20°, encompassing all observable diffraction peaks. Figure 1a shows the evolution of the diffraction patterns

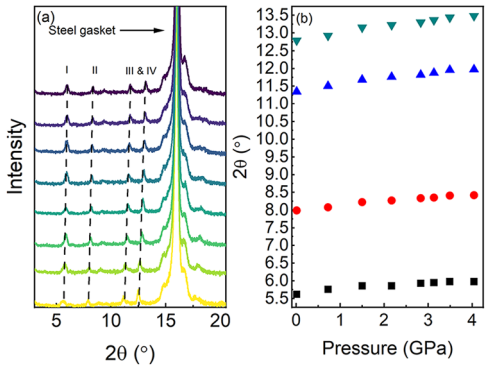

Figure 1. (a) High-pressure XRD patterns of $(4FPEA)_2SnBr_4$ measured between 0.01 and 4.04 GPa. All reflections shift systematically toward higher diffraction angles with increasing pressure, while no additional reflections emerge. (b) Pressure dependence of the 2Θ positions of the four principal reflections.

from 0.01 to 4.04 GPa. With increasing pressure, all reflections shift progressively toward higher 2Θ values, whereas no additional diffraction peaks are detected. The absence of new reflections indicates that no pressure-induced structural phase transition occurs within the investigated pressure range.

A quantitative analysis of the four most intense reflections was carried out, and their positions are summarized in Table S1 in the SI. The pressure dependence of these reflections is presented in Figure 1b. The systematic shift toward higher diffraction angles reflects a continuous lattice compression under hydrostatic pressure.

Because of the absence of reliable crystallographic reference data for $(4FPEA)_2SnBr_4$, refinement of the lattice parameters was not feasible.

To investigate the pressure-dependent optoelectronic response of $(4FPEA)_2SnBr_4$, room-temperature optical transmission measurements were performed. The pronounced red shift of the NBE absorption is attributed to pressure-induced band gap narrowing. Figure 2a presents the optical transmission spectra collected during compression at 300 K. As the pressure increases, the absorption edge shifts continuously toward lower energies, indicating a progressive reduction of the band gap. The pressure dependence of the NBE energy is well described by a linear fit, yielding a pressure coefficient of α_{TR} = −137 ± 7 meV/GPa. No discontinuities or abrupt changes in the pressure dependence of the absorption edge are observed up to 5.05 GPa, suggesting that the electronic structure evolves continuously throughout the investigated pressure range.

The transmission spectra recorded during decompression are presented in Figure 2b. The recovery of the initial absorption edge upon pressure release demonstrates that the pressure-induced band gap narrowing is fully reversible.

https://doi.org/10.1021/acs.jpcc.6c02337
J. Phys. Chem. C XXXX, XXX, XXX−XXX

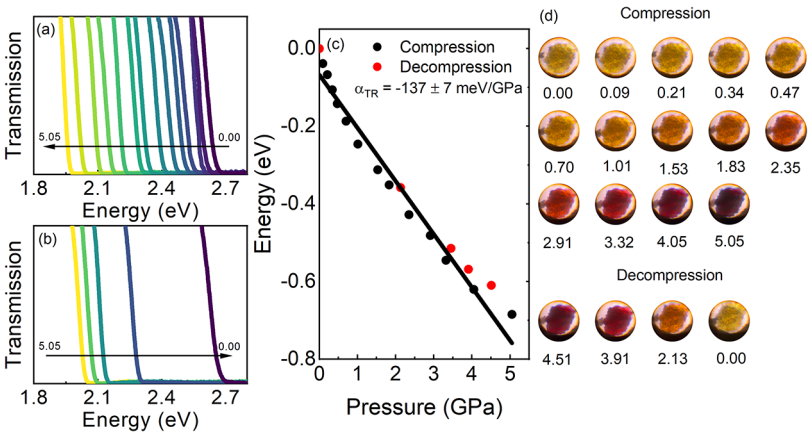

Figure 2. Pressure-dependent optical transmission measurements of $(4FPEA)_2SnBr_4$ at room temperature. (a) Transmission spectra collected during compression. (b) Transmission spectra recorded during decompression. (c) Pressure dependence of the NBE energy extracted from the transmission spectra. (d) Optical micrographs of the sample at selected pressures during compression and decompression.

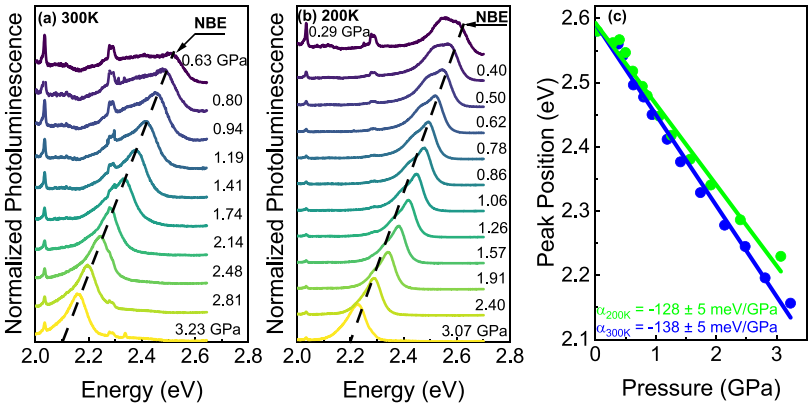

Figure 3. Normalized photoluminescence spectra of $(4FPEA)_2SnBr_4$ under varying hydrostatic pressure at (a) 300 K and (b) 200 K. Free exciton is indicated as NBE, and position changes are marked by a black dashed line. (c) Pressure-induced band gap shift, extracted from the PL spectra at 300 K (blue circles) and 200 K (green circles), along with corresponding linear fits (solid lines). A clear temperature dependence of the pressure coefficient is observed.

Furthermore, the complete restoration of the initial band gap energy indicates that no irreversible structural degradation or pressure-induced amorphization occurs within the investigated pressure range. Figure 2c summarizes the pressure dependence of the NBE energy extracted from the transmission spectra shown in Figure 2a,b.

The band gap decreases continuously with increasing pressure, exhibiting a red shift at a rate of $\alpha_{TR} = -137 \pm 7$ meV/GPa up to 5.05 GPa. Correspondingly, the optical micrographs in Figure 2d reveal a gradual color change from green-yellow at ambient pressure to dark red at 5.05 GPa during compression. This evolution is fully consistent with the spectroscopically observed red shift of the absorption edge and provides direct visual evidence of pressure-induced band gap narrowing.

Figure 3a,b presents the evolution of the normalized PL spectra of $(4FPEA)_2SnBr_4$ under hydrostatic pressure, measured isothermally at 300 and 200 K, respectively. Hydrostatic conditions were maintained up to approximately 3 GPa for all measurements. An assessment of the pressure-transmitting medium is provided in Figure S3 in the SI. At both temperatures, the material retains its initial structural phase throughout the investigated pressure range. The PL response is dominated by NBE emission, with no emergence of additional emissive features, consistent with ambient pressure behavior.[34] Upon increasing pressure, the NBE peak exhibits a pronounced red shift, while its line width and relative intensity remain nearly unchanged compared to low pressures. For clarity in tracking the pressure-induced energy shifts, all spectra are normalized to their maximum intensity. Weak peaks near ~2.3 and 2.0 eV arise from inadvertent illumination by a green and red light source in the experimental environment. However, these artifacts do not affect the determination of the NBE peak position. Pressure coefficients were extracted from linear fits of the NBE peak energy as a function of pressure, with peak positions obtained using Gaussian fitting (Figure 3c). The resulting coefficients are negative and slightly decrease in magnitude with increasing temperature (−138 and −128 meV/GPa at 300 and 200 K, respectively), consistent with pressure-induced band gap narrowing. This behavior reflects enhanced orbital overlap within the Sn−Br framework under compression, which lowers the band edges while preserving the excitonic character of the emission.[24,44] Notably, unlike many halide perovskites, $(4FPEA)_2SnBr_4$ does not exhibit pressure-induced PL enhancement, band gap widening, additional emission channels, or amorphization up to ~3 GPa.[27,45−47] These observations indicate a comparatively rigid pressure response in which compression primarily modifies

https://doi.org/10.1021/acs.jpcc.6c02337
J. Phys. Chem. C XXXX, XXX, XXX−XXX

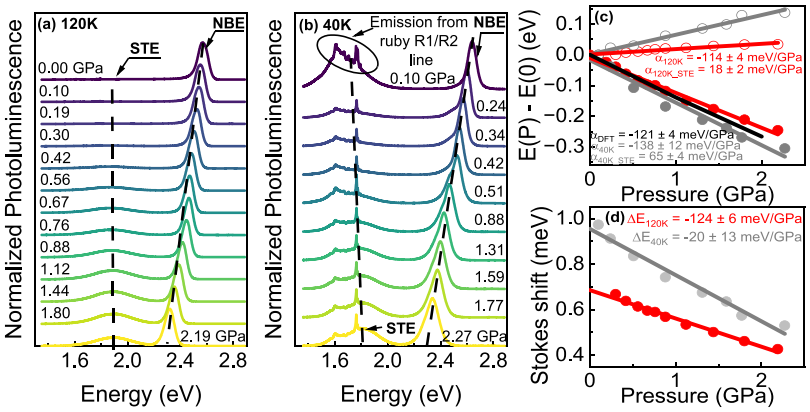

Figure 4. Pressure-dependent normalized PL spectra of $(4FPEA)_2SnBr_4$ at (a) 120 K and (b) 40 K. Self-trapped exciton is indicated as component STE. Position changes are marked by black dashed lines. (c) Pressure-induced band gap shift $\Delta E = E(P) - E(P = 0)$, extracted at 120 K (red circles) and 40 K (gray circles). Solid circles and lines correspond to the NBE feature; open circles and solid lines represent the STE feature. The black line shows DFT calculations (crystal structure is presented in Figure S2 in the SI). (d) Pressure dependence of the Stokes shift from the same data.

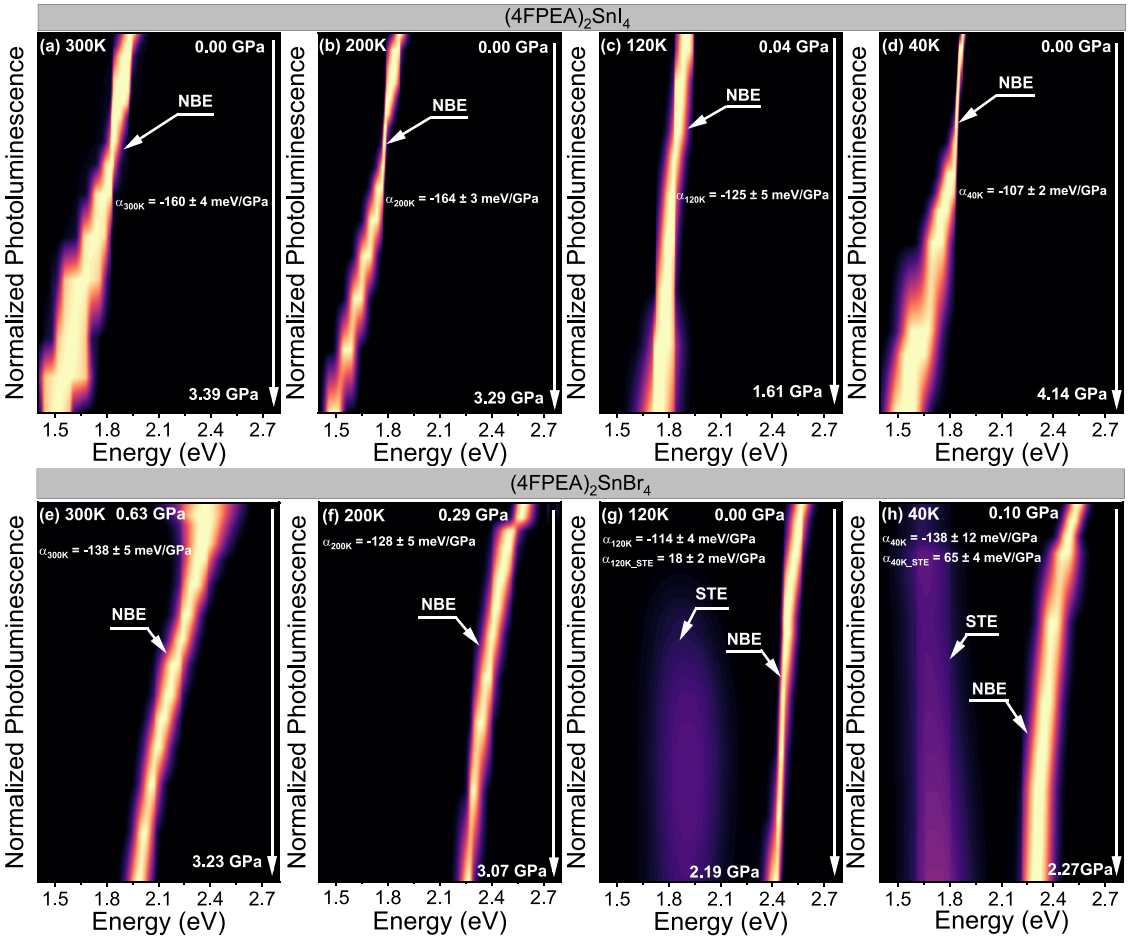

Figure 5. Pressure-dependent photoluminescence spectra of two-layered halide perovskites measured at variable temperature. (a–d) PL spectra of $(4FPEA)_2SnI_4$ collected at 300, 200, 120, and 40 K under hydrostatic pressure. (e–h) Corresponding PL spectra of $(4FPEA)_2SnBr_4$ acquired under identical temperature but different pressure conditions. Bright yellow traces denote the evolution of NBE emission, whereas the violet trace indicates the spectral position of STE emission.

band dispersion rather than activating defect- or polaron-assisted recombination pathways.[28,48,49] In contrast, markedly different PL behavior is observed at lower temperatures.

Figure 4a,b presents the pressure-dependent PL spectra measured at 120 and 40 K. At both temperatures and low pressure, the spectra are dominated by NBE emission, together with a weaker and broader STE band that is separated from NBE emission by a large Stokes shift typical of STE containing small polarons.[19,50] With increasing pressure, the NBE emission undergoes a pronounced red shift, whereas the STE

https://doi.org/10.1021/acs.jpcc.6c02337
J. Phys. Chem. C XXXX, XXX, XXX−XXX

emission exhibits a clear blue shift accompanied by a significant increase in intensity. The opposite pressure response of NBE, which can be attributed to free exciton (FX), and STE emissions highlights their distinct physical origins: while NBE emission follows the band-edge electronic structure, STE emission reflects the depth of the local lattice relaxation potential associated with exciton self-trapping.[51] At 40 K, the STE emission partially overlaps with a secondary peak at 1.78 eV arising from ruby fluorescence used for pressure calibration.[39] Despite this overlap, the pressure-induced blue shift of the STE emission remains unambiguous. Pressure coefficients for both NBE and STE emissions were extracted from linear fits of peak energy versus pressure, with peak positions determined by Gaussian fitting, as shown in Figure 4c. A representative Gaussian fit is provided in Figure S4 in SI. Density functional theory (DFT) results are also included for comparison. At 120 K, the NBE emission exhibits a negative pressure coefficient (−114 meV/GPa), consistent with the trend observed at higher temperatures, while the STE emission shows a positive coefficient (18 meV/GPa). At 40 K, this trend is partially disrupted by the freezing of the pressure-transmitting medium, resulting in quasi-hydrostatic conditions. In addition, the strong pressure-induced enhancement of the STE emission hampers reliable detection of the ruby R1/R2 lines, preventing precise determination of the pressure inside the diamond anvil cell. As a consequence, the NBE pressure coefficient at 40 K is reduced (−138 meV/GPa) and exhibits larger uncertainty. Nevertheless, it agrees well with the DFT-predicted value (−121 meV/GPa), supporting the consistency between experiment and theory (see below Figure 7). The STE emission at 40 K displays a positive pressure coefficient (65 meV/GPa), consistent with pressure-induced STE behavior reported for many halide perovskites.[22,52−54] Up to approximately 2 GPa, no pressure-induced PL enhancement, band gap widening, or amorphization is observed. Importantly, in $(4FPEA)_2SnBr_4$, STE emission becomes pronounced only at low temperatures, confirming its self-trapped nature.[50] Figure 4d presents the pressure dependence of the Stokes shift between NBE and STE emissions. At both temperatures, the Stokes shift decreases monotonically with increasing pressure, reflecting a progressive reduction of the lattice relaxation energy associated with exciton self-trapping. A strong temperature dependence of this effect is observed at 120 K, where the Stokes shift is highly pressure sensitive, exhibiting a slope of −124 meV/GPa, whereas at 40 K, the pressure-induced reduction is much weaker (−20 meV/GPa). This pronounced difference indicates that thermally activated lattice degrees of freedom substantially enhance the pressure response of the NBE−STE energy separation. Upon cooling, lattice stiffening and reduced phonon activity suppress pressure-driven modifications of the self-trapping potential, resulting in a markedly smaller Stokes shift variation.

Temperature- and pressure-dependent PL spectra of the layered perovskites $(4FPEA)_2SnI_4$ and $(4FPEA)_2SnBr_4$ are shown in Figure 5a−d and e−h, respectively, as well as it has been reported for their analogues $MAPbI_3$ and $MAPbBr_3$,[24,55,56] reveal a pronounced halide-dependent exciton localization behavior. At 300 and 200 K, all compounds exhibit a single, relatively narrow emission band attributed to FX recombination, indicating that excitonic states remain predominantly delocalized at elevated temperatures.[57] Upon cooling to 120 K and further to 40 K, an additional low-energy emission band emerges exclusively in the bromide-containing compounds, which we assigned in this paper to STE emission. This emission is absent in the iodide analogues over the entire investigated temperature range. The STE emission is broad (∼350 meV) and strongly red-shifted with respect to the NBE peak, displaying a large Stokes shift that points to a distinct recombination pathway.[20] In addition, STE emission in the bromide perovskites shows a strong sensitivity to hydrostatic pressure. With increasing pressure, its relative intensity increases at the expense of the NBE emission, indicating efficient conversion of photoexcited carriers into localized states.[58] Simultaneously, the NBE emission undergoes a gradual red shift with pressure, whereas the low-energy STE band exhibits an opposite pressure dependence and blue-shifts upon compression. The contrasting pressure coefficients of these two emissions unambiguously demonstrate their different physical origins. The emergence of STE emission at low temperatures indicates that thermal fluctuations suppress stable exciton self-trapping at higher temperatures.[50] The pressure-induced enhancement of STE intensity suggests stabilization of exciton localization driven by strengthened exciton−phonon coupling under lattice compression.[52] At the same time, the blue shift of the STE emission under pressure can be rationalized by a reduction of the lattice relaxation energy due to pressure-induced lattice stiffening.[21] The absence of STE emission in the iodide-based compounds, even at low temperatures and elevated pressures (see Figure S5 in the SI), can be rationalized by their softer lattice and stronger dielectric screening, which disfavor the formation of a stable self-trapped exciton state.[59,60] While a definitive identification would require further experiments, the observed temperature- and pressure-dependent PL behavior provides strong evidence consistent with STE emission in bromide perovskites, highlighting the critical role of lattice rigidity in governing exciton localization in metal-halide perovskites.[61]

Next, we explain the evolution of NBE and STE emissions with temperature and pressure using a configurational-coordinate diagram,[19,21,50,62−64] as shown in Figure 6. In this model, NBE (red) and STE (blue) correspond to distinct energy minima along a lattice distortion coordinate, capturing the dominant exciton−phonon interactions. Optical excitation produces a delocalized NBE state, closely resembling the ground-state lattice. In bromide perovskites, strong exciton−

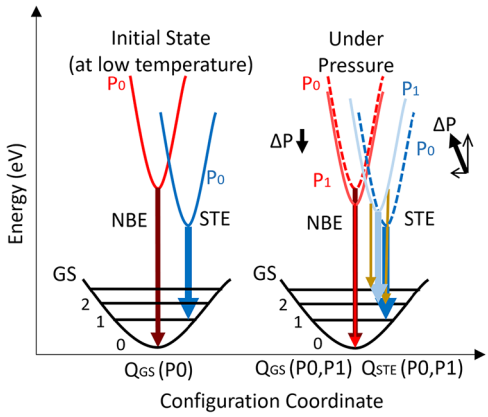

Figure 6. Schematic configuration diagram illustrating the pressure-induced red shift of the NBE emission and blue shift of STE emission in $(4FPEA)_2SnBr_4$. P_0 denotes ambient pressure, while P_1 larger than P_0 represents elevated pressure. GS indicates the ground state of the system.

https://doi.org/10.1021/acs.jpcc.6c02337
J. Phys. Chem. C XXXX, XXX, XXX−XXX

phonon coupling drives relaxation into a shifted STE minimum, producing broad, strong Stokes-shifted emission. Thermal activation over the barrier separating NBE and STE states governs their relative populations, explaining why STE emission dominates at low temperatures. Hydrostatic pressure reshapes the energy landscape, promoting exciton self-trapping and stiffening the lattice, which enhances the STE population. Notably, we observe that the Stokes shift decreases with increasing pressure. This behavior can be attributed to a reduction in the lattice relaxation energy, reflecting a pressure-induced change in the energy formation of small polarons. Consequently, STE emission exhibits a pressure-induced blue shift, in contrast to the gradual red shift of NBE emission. In iodide analogues, STE emission is absent (see Figure S5 in SI showing the PL spectrum of $(4FPEA)_2SnI_4$ at 40 K and ambient pressure (0 GPa) plotted on a logarithmic scale), as the softer lattice and stronger dielectric screening suppress exciton self-trapping. Displacement along the configurational coordinate reflects lattice relaxation energy, which can be quantitatively inferred from the Stokes shift. These observations underscore the critical role of lattice rigidity and exciton−phonon coupling in controlling exciton self-trapping, while also revealing how external pressure can be used to tune polaron formation and the associated emission properties in layered halide perovskites.

To contextualize the experimental pressure response within an electronic structure framework, we performed DFT calculations of the pressure-dependent band structure of $(4FPEA)_2SnBr_4$. As shown in Figure 7, the material retains a direct band gap up to 3 GPa, demonstrating the robustness of the band edge under moderate hydrostatic compression. Increasing the pressure induces a pronounced band gap reduction, consistent with enhanced orbital overlap and lattice compression within the inorganic Sn−Br framework. The calculated band gap pressure coefficient (−121 meV/GPa) closely matches the experimentally extracted NBE pressure coefficient, providing strong evidence that the pressure evolution of the NBE emission is governed predominantly by band edge renormalization. By contrast, the exciton binding energy exhibits only a weak pressure dependence, indicating that changes in excitonic Coulomb interactions play a secondary role. This clear separation of energy scales demonstrates that the anomalous pressure response of the STE emission cannot originate from band-edge effects but instead arises from pressure-induced modifications of lattice relaxation and exciton self-trapping energetics, as captured by the configurational-coordinate model.

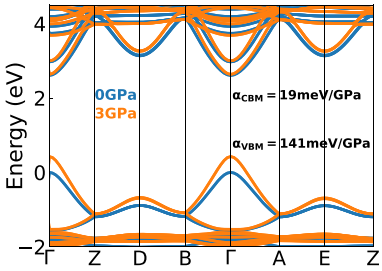

Figure 7. Pressure-dependent band structures of $(4FPEA)_2SnBr_4$ at 0 and 3 GPa, revealing a persistent direct band gap and a significant pressure-induced red shift. Values of pressure coefficients for VBM and CBM are also given.

CONCLUSIONS

In conclusion, we have demonstrated $(4FPEA)_2SnBr_4$ as a model system for elucidating the interplay between lattice dynamics and exciton localization in 2D tin-halide perovskites. The contrasting pressure responses of NBE and STE reveal that exciton−phonon coupling and lattice rigidity can be systematically tuned to control polaron formation and energy relaxation pathways. The absence of STE in iodide analogue $(4FPEA)_2SnI_4$ underscores the delicate balance between lattice stiffness and dielectric screening in stabilizing self-trapped states. More broadly, our findings demonstrate that external perturbations such as hydrostatic pressure can serve as a precise probe of polaronic phenomena, advancing fundamental understanding and guiding the rational design of next-generation lead-free perovskite materials.

ASSOCIATED CONTENT

Supporting Information

The Supporting Information is available free of charge at https://pubs.acs.org/doi/10.1021/acs.jpcc.6c02337.

XRD pattern of the $(4FPEA)_2SnBr_4$ microcrystals and material measured under ambient conditions; crystal structure of $(4FPEA)_2SnBr_4$ used in DFT simulations; comment about hydrostaticity of Daphne 7575; example of Gaussian fitting; photoluminescence spectrum of $(4FPEA)_2SnI_4$ and $(4FPEA)_2SnBr_4$ at 40 K and ambient pressure plotted on a logarithmic intensity scale; positions of the four main reflections as a function of pressure for $(4FPEA)_2SnBr_4$ (PDF)

AUTHOR INFORMATION

Corresponding Author

Rafał Bartoszewicz − *Department of Semiconductor Materials Engineering, Wrocław University of Science and Technology, 50-370 Wrocław, Poland;* orcid.org/0009-0001-2951-1459; Email: rafal.bartoszewicz@pwr.edu.pl

Authors

Jakub Ziembicki − *Department of Semiconductor Materials Engineering, Wrocław University of Science and Technology, 50-370 Wrocław, Poland*

Ewelina Zdanowicz − *Department of Semiconductor Materials Engineering, Wrocław University of Science and Technology, 50-370 Wrocław, Poland;* orcid.org/0000-0001-7479-6943

Artur P. Herman − *Department of Semiconductor Materials Engineering, Wrocław University of Science and Technology, 50-370 Wrocław, Poland;* orcid.org/0000-0002-1393-0317

Jarosław Serafińczuk − *Department of Semiconductor Materials Engineering, Wrocław University of Science and Technology, 50-370 Wrocław, Poland;* orcid.org/0000-0001-9809-4233

Jesús Sánchez-Diaz − *Institute of Advanced Materials (INAM), Castellón de la Plana 12006, Spain*

Samrat Das Adhikari − *Institute of Advanced Materials (INAM), Castellón de la Plana 12006, Spain; Institute of Physical Chemistry, Polish Academy of Sciences, 01-224 Warsaw, Poland;* orcid.org/0000-0002-5670-5179

https://doi.org/10.1021/acs.jpcc.6c02337
J. Phys. Chem. C XXXX, XXX, XXX−XXX

Iván Mora-Seró − *Institute of Advanced Materials (INAM), Castellón de la Plana 12006, Spain;* orcid.org/0000-0003-2508-0994

Robert Kudrawiec − *Department of Semiconductor Materials Engineering, Wrocław University of Science and Technology, 50-370 Wrocław, Poland;* orcid.org/0000-0003-2593-9172

Complete contact information is available at: https://pubs.acs.org/10.1021/acs.jpcc.6c02337

Notes

The authors declare no competing financial interest.

■ ACKNOWLEDGMENTS

This work was financed by the National Science Centre (NC) Poland under OPUS 29 grant no. 2025/57/B/ST3/03683. This work was partially funded by the Ministerio de Ciencia e Innovación of the Spanish Government by the project PLEDs, PID2022-140090OB-C21/AEI/10.13039/501100011033/FEDER. Calculations have been carried out using resources provided by Wroclaw Centre for Networking and Supercomputing (https://wcss.pl).

■ REFERENCES

(1) Jokar, E.; Cai, L.; Han, J.; Nacpil, E. J. C.; Jeon, I. Emerging Opportunities in Lead-Free and Lead-Tin Perovskites for Environmentally Viable Photodetector Applications. *Chem. Mater.* **2023**, *35*, 3404−3426.

(2) Li, X.-Z.; Ye, Y.; Cao, Y.; Zhang, D.; Lin, Y.; Chang, J.; Zhu, L.; Wang, N.; Huang, W.; Wang, J. Tin-halide perovskites for light-emitting diodes. *Chem. Soc. Rev.* **2025**, *54*, 6697−6725.

(3) Abate, A. Stable Tin-Based Perovskite Solar Cells. *ACS Energy Lett.* **2023**, *8*, 1896−1899.

(4) Zhao, D.; Yu, Y.; Wang, C.; Liao, W.; Shrestha, N.; Grice, C. R.; Cimaroli, A. J.; Guan, L.; Ellingson, R. J.; Zhu, K.; Zhao, X.; Xiong, R.-G.; Yan, Y. Low-bandgap mixed tin-lead iodide perovskite absorbers with long carrier lifetimes for all-perovskite tandem solar cells. *Nat. Energy* **2017**, *2*, No. 17018.

(5) Li, Y.; Wang, D.; Yang, Y.; Ding, C.; Hu, Y.; Liu, F.; Wei, Y.; Liu, D.; Li, H.; Shi, G.; Chen, S.; Li, H.; Fuchimoto, A.; Tosa, K.; Hiroki, U.; Hayase, S.; Wei, H.; Shen, Q. Stable Inorganic Colloidal Tin and Tin-Lead Perovskite Nanocrystals with Ultralong Carrier Lifetime via Sn(IV) Control. *J. Am. Chem. Soc.* **2024**, *146*, 3094−3101.

(6) Galve-Lahoz, S.; Sánchez-Diaz, J.; Aktas, E.; Rodriguez-Pereira, J.; Abate, A.; Delgado, J. L.; Mora-Seró, I. Reducing Nonradiative Recombination Losses in Tin-Based Perovskite LEDs Utilizing a Self-Assembled Monolayer. *ACS Appl. Mater. Interfaces* **2025**, *17*, 60937−60943.

(7) Chakraborty, R.; Paul, G.; Pal, A. J. Quantum Confinement and Dielectric Deconfinement in Quasi-Two-Dimensional Perovskites: Their Roles in Light-Emitting Diodes. *Phys. Rev. Appl.* **2022**, *17*, No. 054045.

(8) Hansen, K. R.; McClure, C. E.; Powell, D.; Hsieh, H.-C.; Flannery, L.; Garden, K.; Miller, E. J.; King, D. J.; Sainio, S.; Nordlund, D.; Colton, J. S.; Whittaker-Brooks, L. Low Exciton Binding Energies and Localized Exciton-Polaron States in 2D Tin Halide Perovskites. *Adv. Opt. Mater.* **2022**, *10*, No. 2102698.

(9) Chen, Y.; Wang, Z.; Wei, Y.; Liu, Y.; Hong, M. Exciton Localization for Highly Luminescent Two-Dimensional Tin-Based Hybrid Perovskites through Tin Vacancy Tuning. *Angew. Chem., Int. Ed.* **2023**, *62*, No. e202301684.

(10) Zhang, T.; Zhou, C.; Feng, X.; Dong, N.; Chen, H.; Chen, X.; Zhang, L.; Lin, J.; Wang, J. Regulation of the luminescence mechanism of two-dimensional tin halide perovskites. *Nat. Commun.* **2022**, *13*, No. 60.

(11) Straus, D. B.; Kagan, C. R. Electrons, Excitons, and Phonons in Two-Dimensional Hybrid Perovskites: Connecting Structural, Optical, and Electronic Properties. *J. Phys. Chem. Lett.* **2018**, *9*, 1434−1447.

(12) Jin, L.; Mora Perez, C.; Gao, Y.; Ma, K.; Park, J. Y.; Li, S.; Guo, P.; Dou, L.; Prezhdo, O.; Huang, L. Superior Phonon-Limited Exciton Mobility in Lead-Free Two-Dimensional Perovskites. *Nano Lett.* **2024**, *24*, 3638−3646.

(13) Srimath Kandada, A. R.; Silva, C. Exciton Polarons in Two-Dimensional Hybrid Metal-Halide Perovskites. *J. Phys. Chem. Lett.* **2020**, *11*, 3173−3184.

(14) Duan, J.; Li, J.; Divitini, G.; Cortecchia, D.; Yuan, F.; You, J.; Liu, S. F.; Petrozza, A.; Wu, Z.; Xi, J. 2D Hybrid Perovskites: From Static and Dynamic Structures to Potential Applications. *Adv. Mater.* **2024**, *36*, No. 2403455.

(15) Zhou, H.; Feng, Q.; Sun, C.; Li, Y.; Tao, W.; Tang, W.; Li, L.; Shi, E.; Nan, G.; Zhu, H. Robust excitonic light emission in 2D tin halide perovskites by weak excited state polaronic effect. *Nat. Commun.* **2024**, *15*, No. 8541.

(16) Tao, W.; Zhang, Y.; Zhu, H. Dynamic Exciton Polaron in Two-Dimensional Lead Halide Perovskites and Implications for Optoelectronic Applications. *Acc. Chem. Res.* **2022**, *55*, 345−353.

(17) Gualdrón-Reyes, A. F. Self-Trapped Exciton versus Band-Edge Electron Transitions: Insights of the Factors Affecting the Optical Properties of Lead-Free Sn-Halide Perovskites. *Adv. Opt. Mater.* **2025**, *13*, No. 2402043.

(18) Li, J.; Wang, H.; Li, D. Self-trapped excitons in two-dimensional perovskites. *Front. Optoelectron.* **2020**, *13*, 225−234.

(19) Li, S.; Luo, J.; Liu, J.; Tang, J. Self-Trapped Excitons in All-Inorganic Halide Perovskites: Fundamentals, Status, and Potential Applications. *J. Phys. Chem. Lett.* **2019**, *10*, 1999−2007.

(20) Pan, F.; Li, J.; Ma, X.; Nie, Y.; Liu, B.; Ye, H. Free and Self-Trapped Exciton Emission in Perovskite $CsPbBr_3$ Microcrystals. *RSC Adv.* **2021**, *12*, 1035−1042.

(21) Dai, S.; Xing, X.; Hadjiev, V. G.; Qin, Z.; Tong, T.; Yang, G.; Wang, C.; Hou, L.; Deng, L.; Wang, Z.; Feng, G.; Bao, J. Theory and experiments of pressure-tunable broadband light emission from self-trapped excitons in metal halide crystals. *Mater. Today Phys.* **2023**, *30*, No. 100926.

(22) Mączka, M.; Sobczak, S.; Roszak, K.; Vasconcelos, D. L. M.; Dybała, F.; Herman, A. P.; Kudrawiec, R.; Katrusiak, A.; Freire, P. T. C. Pressure-Induced Detrapping from Self-Trapped Excitons to Free Excitons toward Enhanced Emission and Piezochromism in Ruddlesden-Popper (110)-Oriented Perovskites. *ACS Appl. Mater. Interfaces* **2025**, *17*, 58452−58466.

(23) Jaffe, A.; Lin, Y.; Karunadasa, H. I. Halide Perovskites under Pressure: Accessing New Properties through Lattice Compression. *ACS Energy Lett.* **2017**, *2*, 1549−1555.

(24) Bartoszewicz, R.; Ziembicki, J.; Zdanowicz, E.; Herman, A. P.; Serafińczuk, J.; Sánchez-Diaz, J.; Das Adhikari, S.; Mora-Seró, I.; Kudrawiec, R. Giant Band Gap Narrowing under Hydrostatic Pressure in (4FP)2SnI4 Halide Perovskite. *J. Phys. Chem. Lett.* **2025**, *16*, 6372−6377.

(25) Kong, L.; Gong, J.; Spanopoulos, I.; Yan, S.; Li, Z.; Zhu, Z.; Liu, X.; Zhu, Y.; Dong, H.; Shu, H.; Hu, Q.; Yang, W.; Mao, H.-k.; Kanatzidis, M. G.; Liu, G. Revealing the Universal Pressure-Driven Behavior of Hybrid Halide Perovskites and Unique Optical Modifiability in Extremely Soft 2D Tin-Based System. *Adv. Funct. Mater.* **2024**, *34*, No. 2414437.

(26) Fang, Y.-S.; Guo, Y.-F.; Xu, H.-J.; Chen, X.-G.; Zhou, L.; Wang, Z.-X.; Tang, Y.-Y.; Qin, Y. Pressure-Modulated Near-Infrared Photoluminescence of a Two-Dimensional Germanium Halide Perovskite. *J. Phys. Chem. Lett.* **2025**, *16*, 10126−10133.

(27) Zhao, W.; Xiao, G.; Zou, B. Pressure-induced emission (PIE) in halide perovskites toward promising applications in scintillators and solid-state lighting. *Aggregate* **2024**, *5*, No. e461.

(28) Dybała, F.; Kudrawiec, R.; Polak, M. P.; Herman, A. P.; Sieradzki, A.; Mączka, M. Near-bandgap emission in [HOC2H4NH3]2PbI4 perovskite under hydrostatic pressure:

emission of a free exciton and a polaronic exciton. *Mater. Adv.* **2025**, *6*, 569−578.
(29) Zhumekenov, A. A.; Saidaminov, M. I.; Mohammed, O. F.; Bakr, O. M. Stimuli-responsive switchable halide perovskites: Taking advantage of instability. *Joule* **2021**, *5*, 2027−2046.
(30) Sun, Y.; Ge, L.; Dai, L.; Cho, C.; Ferrer Orri, J.; Ji, K.; Zelewski, S. J.; Liu, Y.; Mirabelli, A. J.; Zhang, Y.; Huang, J.-Y.; Wang, Y.; Gong, K.; Lai, M. C.; Zhang, L.; Yang, D.; Lin, J.; Tennyson, E. M.; Ducati, C.; Stranks, S. D.; Cui, L.-S.; Greenham, N. C. Bright and stable perovskite light-emitting diodes in the near-infrared range. *Nature* **2023**, *615*, 830−835.
(31) Liu, G.; Kong, L.; Yang, W.; Mao, H.-k. Pressure engineering of photovoltaic perovskites. *Mater. Today* **2019**, *27*, 91−106.
(32) Zhu, Y.; Buitenhuis, J.; Förster, B.; Vetrano, M. R.; Koos, E. Development of Perovskite Quantum Dots for Two-Dimensional Temperature Sensors. *ACS Appl. Nano Mater.* **2023**, *6*, 4661−4671.
(33) Vescio, G.; Dirin, D. N.; González-Torres, S.; Sanchez-Diaz, J.; Vidal, R.; Franco, I. P.; Adhikari, S. D.; Chirvony, V. S.; Martínez-Pastor, J. P.; Vinocour Pacheco, F. A.; Przypis, L.; Öz, S.; Hernández, S.; Cirera, A.; Mora-Seró, I.; Kovalenko, M. V.; Garrido, B. Inkjet-Printed Red-Emitting Flexible LEDs Based on Sustainable Inks of Layered Tin Iodide Perovskite. *Adv. Sustainable Syst.* **2024**, *8*, No. 2400060.
(34) Sanchez-Diaz, J.; Rodriguez-Pereira, J.; Das Adhikari, S.; Mora-Seró, I. Synthesis of Hybrid Tin-Based Perovskite Microcrystals for LED Applications. *Adv. Sci.* **2024**, *11*, No. 2403835.
(35) Romani, L.; Bala, A.; Kumar, V.; Speltini, A.; Milella, A.; Fracassi, F.; Listorti, A.; Profumo, A.; Malavasi, L. PEA2SnBr4: a water-stable lead-free two-dimensional perovskite and demonstration of its use as a co-catalyst in hydrogen photogeneration and organic-dye degradation. *J. Mater. Chem. C* **2020**, *8*, 9189−9194.
(36) Hazra, V.; Mandal, A.; Bhattacharyya, S. Optoelectronic insights of lead-free layered halide perovskites. *Chem. Sci.* **2024**, *15*, 7374−7393.
(37) Shen, G.; Wang, Y.; Dewaele, A.; Wu, C.; Fratanduono, D. E.; Eggert, J.; Klotz, S.; Dziubek, K. F.; Loubeyre, P.; Fat'yanov, O. V.; Asimow, P. D.; Mashimo, T.; W, R. M. M. Toward an international practical pressure scale: A proposal for an IPPS ruby gauge (IPPS-Ruby2020). *High Pressure Res.* **2020**, *40*, 299−314.
(38) Datchi, F.; Dewaele, A.; Loubeyre, P.; Letoullec, R.; Godec, Y. L.; Canny, B. Optical pressure sensors for high-pressure-high-temperature studies in a diamond anvil cell. *High Pressure Res.* **2007**, *27*, 447−463.
(39) Kresse, G.; Hafner, J. Ab initio molecular dynamics for liquid metals. *Phys. Rev. B* **1993**, *47*, No. 558.
(40) Kresse, G.; Furthmüller, J. Efficient iterative schemes for ab initio total-energy calculations using a plane-wave basis set. *Phys. Rev. B* **1996**, *54*, 11169−11186.
(41) Kresse, G.; Furthmüller, J. Efficiency of ab-initio total energy calculations for metals and semiconductors using a plane-wave basis set. *Comput. Mater. Sci.* **1996**, *6*, 15−50.
(42) Kresse, G.; Joubert, D. From ultrasoft pseudopotentials to the projector augmented-wave method. *Phys. Rev. B* **1999**, *59*, 1758−1775.
(43) Ning, J.; Kothakonda, M.; Furness, J. W.; Kaplan, A. D.; Ehlert, S.; Brandenburg, J. G.; Perdew, J. P.; Sun, J. Workhorse minimally empirical dispersion-corrected density functional with tests for weakly bound systems: r^{2}SCAN + rVV10. *Phys. Rev. B* **2022**, *106*, No. 075422.
(44) Coduri, M.; Shiell, T. B.; Strobel, T. A.; Mahata, A.; Cova, F.; Mosconi, E.; De Angelis, F.; Malavasi, L. Origin of pressure-induced band gap tuning in tin halide perovskites. *Mater. Adv.* **2020**, *1*, 2840−2845.
(45) Wu, K.; Bera, A.; Ma, C.; Du, Y.; Yang, Y.; Li, L.; Wu, T. Temperature-dependent excitonic photoluminescence of hybrid organometal halide perovskite films. *Phys. Chem. Chem. Phys.* **2014**, *16*, 22476−22481.
(46) Samanta, D.; Chaudhary, S. P.; Ghosh, B.; Bhattacharyya, S.; Shukla, G.; Mukherjee, G. D. Pressure-induced emission enhancement and bandgap narrowing: Experimental investigations and first-principles theoretical simulations on the model halide perovskite $Cs_3Sb_2Br_9$. *Phys. Rev. B* **2022**, *105*, No. 104103.
(47) Lü, X.; Wang, Y.; Stoumpos, C. C.; Hu, Q.; Guo, X.; Chen, H.; Yang, L.; Smith, J. S.; Yang, W.; Zhao, Y.; Xu, H.; Kanatzidis, M. G.; Jia, Q. Enhanced Structural Stability and Photo Responsiveness of CH3NH3SnI3 Perovskite via Pressure-Induced Amorphization and Recrystallization. *Adv. Mater.* **2016**, *28*, 8663−8668.
(48) Yang, B.; Bogachuk, D.; Suo, J.; Wagner, L.; Kim, H.; Lim, J.; Hinsch, A.; Boschloo, G.; Nazeeruddin, M. K.; Hagfeldt, A. Strain effects on halide perovskite solar cells. *Chem. Soc. Rev.* **2022**, *51*, 7509−7530.
(49) Wu, J.; Liu, S.-C.; Li, Z.; Wang, S.; Xue, D.-J.; Lin, Y.; Hu, J.-S. Strain in perovskite solar cells: origins, impacts and regulation. *Natl. Sci. Rev.* **2021**, *8*, No. nwab047.
(50) Han, Y.; Cheng, X.; Cui, B.-B. Factors influencing self-trapped exciton emission of low-dimensional metal halides. *Mater. Adv.* **2023**, *4*, 355−373.
(51) Xu, B.; Li, Y.; Hong, P.; Zhang, P.; Han, J.; Xiao, Z.; Quan, Z. Pressure-controlled free exciton and self-trapped exciton emission in quasi-one-dimensional hybrid lead bromides. *Nat. Commun.* **2024**, *15*, No. 7403.
(52) Jing, X.; Sun, R.; Tian, H.; Liu, R.; Liu, B.; Zhou, D.; Li, Q.; Liu, B. Evolution of self-trapped exciton emission tuned by high pressure in 2D all-inorganic cesium lead halide nanosheets. *J. Mater. Chem. C* **2022**, *10*, 8711−8718.
(53) Gao, F.-F.; Qin, Y.; Li, Z.-G.; Li, W.; Hao, J.; Li, X.; Liu, Y.; Howard, C. J.; Wu, X.; Jiang, X.; Lin, Z.; Lu, P.; Bu, X.-H. Unusual Pressure-Induced Self-Trapped Exciton to Free Exciton Transfer in Chiral 2D Lead Bromide Perovskites. *ACS Nano* **2024**, *18*, 3251−3259.
(54) Shi, H.; Chen, L.; Moutaabbid, H.; Feng, Z.; Zhang, G.; Wang, L.; Li, Y.; Guo, H.; Liu, C. Mechanism of Pressure-Modulated Self-Trapped Exciton Emission in Cs2TeCl6 Double Perovskite. *Small* **2024**, *20*, No. 2405692.
(55) Pieniążek, A.; Dybała, F.; Polak, M. P.; Przypis, L.; Herman, A. P.; Kopaczek, J.; Kudrawiec, R. Bandgap Pressure Coefficient of a CH3NH3PbI3 Thin Film Perovskite. *J. Phys. Chem. Lett.* **2023**, *14*, 6470−6476.
(56) Pieniążek, A.; Dybała, F.; Przypis, L.; Polak, M. P.; Norek, M.; Kowalski, B. J.; Kudrawiec, R. Beyond the Cubic Phase: Pressure-Induced Bandgap Modulation in a CH3NH3PbBr3 Perovskite at Low Temperatures. *Adv. Opt. Mater.* **2026**, *14*, No. e03177.
(57) Tan, J.; Zhou, Y.; Lu, D.; Feng, X.; Liu, Y.; Zhang, M.; Lu, F.; Huang, Y.; Xu, X. Temperature-dependent photoluminescence of lead-free cesium tin halide perovskite microplates. *Chin. Phys. B* **2023**, *32*, No. 117802.
(58) Rong, Y.; Wang, L.; Wang, Y.; Wang, W.; Wang, J.; Yuan, Y.; Shahzadi, U.; Chen, J.; Zhang, L.; Wang, K.; Guo, H. Pressure-Induced Unusual Transition of Luminescence Mechanics from Self-Trapped Exciton to Free Exciton Emission in Lead Bromide Perovskitoids. *Adv. Opt. Mater.* **2025**, *13*, No. 2402086.
(59) Gautier, R.; Paris, M.; Massuyeau, F. Exciton Self-Trapping in Hybrid Lead Halides: Role of Halogen. *J. Am. Chem. Soc.* **2019**, *141*, 12619−12623.
(60) Xing, Y.; Yin, J.; Qiao, Y.; Zhao, J.; He, H.; Zhao, D.; Zhang, W.; Mei, S.; Guo, R. Gram-Scale Synthesis and Optical Properties of Self-Trapped-Exciton-Emitting Two-Dimensional Tin Halide Perovskites. *Nanomaterials* **2025**, *15*, No. 818, DOI: 10.3390/nano15110818.
(61) Liang, Y.; Jiang, Y.; Du, K.-Z.; Lin, Y.-P.; Ma, X.; Qiu, D.; Wang, Z.; Hou, Y.; Wei, X.; Zhang, Q. A High-Rigidity Organic-Inorganic Metal Halide Hybrid Enabling Reversible and Enhanced Self-Trapped Exciton Emission under High Pressure. *Nano Lett.* **2023**, *23*, 7599−7606.
(62) Zhao, W.; Fu, R.; Yang, J.; Xiao, G.; Zou, B. Building New Structural Distortion Descriptors through Pressure Engineering toward Enhanced Violet Emission in 2D Hybrid Perovskite. *Adv. Opt. Mater.* **2024**, *12*, No. 2401732.

(63) Yu, X.; Fang, Y.; Sun, X.; Xie, Y.; Liu, C.; Wang, K.; Xiao, G.; Zou, B. Pressure-Tuning Localized Excitons Toward Enhanced Emission, Photocurrent Enhancement and Piezochromism in Unconventional ACI-Type 2D Hybrid Perovskites. *Angew. Chem., Int. Ed.* **2024**, *63*, No. e202412756.
(64) Ma, Z.; Lv, P.; He, X.; Wang, F.; Li, Y.; Xiao, G.; Zou, B. Self-Trapped Excitons or Bi3+ Ions for Broad Emission in a Lead-Free Double Perovskite? Hearing What Pressure Says. *Nano Lett.* **2025**, *25*, 9345−9352.

https://doi.org/10.1021/acs.jpcc.6c02337
J. Phys. Chem. C XXXX, XXX, XXX−XXX